Case Studies in Thermal Engineering 76 (2025) 107272

Contents lists available at ScienceDirect

Case Studies in Thermal Engineering

journal homepage: www.elsevier.com/locate/csite

Preliminary design and thermal evaluation of a hexagonal pulsating heat pipe for fuel cell applications

Friedrich Franke *, Markus Kober, Stefan Kazula

German Aerospace Center (DLR), Institute of Electrified Aero Engines, Lieberoser Straße 13a, Cottbus, Germany

GRAPHICAL ABSTRACT

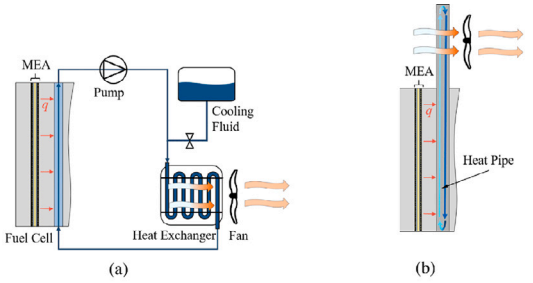

Schematics of a conventional liquid-based Thermal Management system (a) and a proposed Pulsating Heat Pipe (PHP) approach (b)

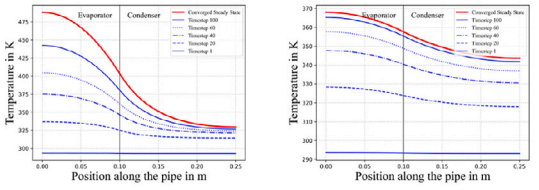

Temperature Distributions across a 1D Section of passive Coolant Elements with equivalent thermal Conductivities of (a): 401W/mK and (b): 3300 W/mK

ARTICLE INFO

Keywords:
Thermal management
Feasibility study
HT-PEM fuel cell

ABSTRACT

As the world transitions away from fossil fuels, alternative methods of energy storage and conversion are in the center of many research endeavours. Aviation poses a unique challenge for decarbonization due to the demand for high specific energy and power density of the aircraft

* Corresponding author.
E-mail address: friedrich.franke@dlr.de (F. Franke).

https://doi.org/10.1016/j.csite.2025.107272
Received 3 June 2025; Received in revised form 8 October 2025; Accepted 18 October 2025
Available online 30 October 2025

Electric aircraft propulsion

propulsion system. Hydrogen-electric technologies employing fuel cells, are among the most promising approaches for achieving zero-emission flight.

However, thermal management of fuel cell systems remains a significant challenge due to the limitations of conventional liquid cooling architectures. These systems require bulky heat exchangers and consume substantial parasitic power, and consist of multiple subsystems, adding complexity to the propulsion system.

To address these challenges, this study proposes integrating novel hexagonal pulsating heat pipes into a High Temperature Polymer Electrolyte Membrane fuel cell stack to transfer heat from the center of the stack and reject it to an external airflow. The research aims to determine whether this approach can reliably control the fuel cell's operating temperature, while potentially reducing system weight, complexity, and reliance on parasitic power.

The thermal performance of the proposed system is evaluated based on equivalent thermal conductivity measurements from literature. To minimize computational demand, a singular pipe simplification is developed and its thermal behavior investigated numerically and analytically. The results demonstrate that, under some conditions, the heat pipe system is able to keep the fuel cell's operating temperatures below 200 °C. A parameter study is conducted to evaluate the effects of heat pipe length, external air flow speed and equivalent thermal conductivity on the thermal performance.

As an exemplary case from the parametric study, a configuration with a condenser length of 5 cm, coolant air speed of 3 $m\,s^{-1}$, and an equivalent thermal conductivity of 3300 $W\,m^{-1}\,K^{-1}$ yielded a maximum cell temperature of 140 °C and a temperature difference of 10.2 °C across the 10 cm-long cell, highlighting the theoretical feasibility of the concept.

1. Introduction

To reduce the impact of man made climate change, alternative methods of energy storage and conversion have become the focus of scientific and industrial interest. One approach of storing energy is utilizing hydrogen as a versatile and sustainable energy carrier.

Hydrogen can be converted back into electrical energy using fuel cells. In such a cell, the reactants hydrogen and oxygen are supplied through channels in the bipolar plates (BPPs), which serve as the mechanical frame and current collectors of the system. From these channels, the gases are distributed through the diffusion layers to the catalyst layers, where the electrochemical reactions occur. On the anode side of the cell, hydrogen is oxidized using a catalyst, generating free protons and electrons. The protons migrate through the polymer membrane in the center of the cell and recombine with the oxygen and free electrons on the cathode side to form water molecules. Through this transition of charge, an electrical potential between the bipolar plates is generated, resulting in the flow of current and the generation of the electrical power P_{el}.

During the operation of the fuel cell, about half of the energy from the redox reactions emerges in the form of parasitic heat and needs to be rejected from the system to prevent overheating. The ideal operating temperature varies between fuel cell types. For High Temperature Polymer Electrolyte (HT-PEM) Fuel cells, which are the selected fuel cell type for this work, the ideal temperature ranges from 120 to 200 °C, depending on the specific properties of the Membrane Electrode Assembly (MEA). The MEA consists of the membrane, the diffusion layers and the catalyst layers [1, pp. 441].

Currently, most high-power fuel cell stacks are cooled using a liquid-based Thermal Management System (TMS) that pumps a liquid coolant through channels inside the fuel cell stack, where the coolant heats up, absorbing heat from the MEA [2–4]. The warmed liquid is then fed through a liquid-to-air heat exchanger, where it is cooled and subsequently fed back to a reservoir. This architecture, depicted in Fig. 1(a), is capable of removing large amounts of heat, but requires a complex system of many heavy components and consumes significant amounts of parasitic power for the generation of sufficient cooling air flow in the heat exchanger and the pumping of the liquid coolant [5,6]

However, certain applications such as aviation, impose high requirements on the power-to-weight and power-to-volume ratios, as well as on the safety and reliability of a fuel-cell system. These demanding criteria highlight the importance of exploring alternative thermal management strategies.

Consequently, there is a clear need for thermal management solutions that combine high heat removal capacity with low mass, compact integration, and minimal parasitic power consumption.

A variety of alternatives to liquid cooling for fuel cells exist. These include air cooling, via the cathode or separate flow channels [7–9], phase change cooling [5,10] or passive cooling with solid heat spreaders [11,12] or heat pipes in various forms [13–16].

A heat pipe is a closed two-phase heat transfer system that leverages the latent heat of evaporation, as well as capillary forces to transfer heat from one end of the system to the other.

This approach presents a particularly promising technology for aviation applications due to the combination of high heat transfer performance, low system mass, and operational reliability [17]. Compared to other passive solutions, such as those based on pyrolytic graphite [18,19], heat pipes generally provide superior heat transfer rates and provide greater mechanical stability and resilience. For this reason, they have been chosen as the focus of further investigation.

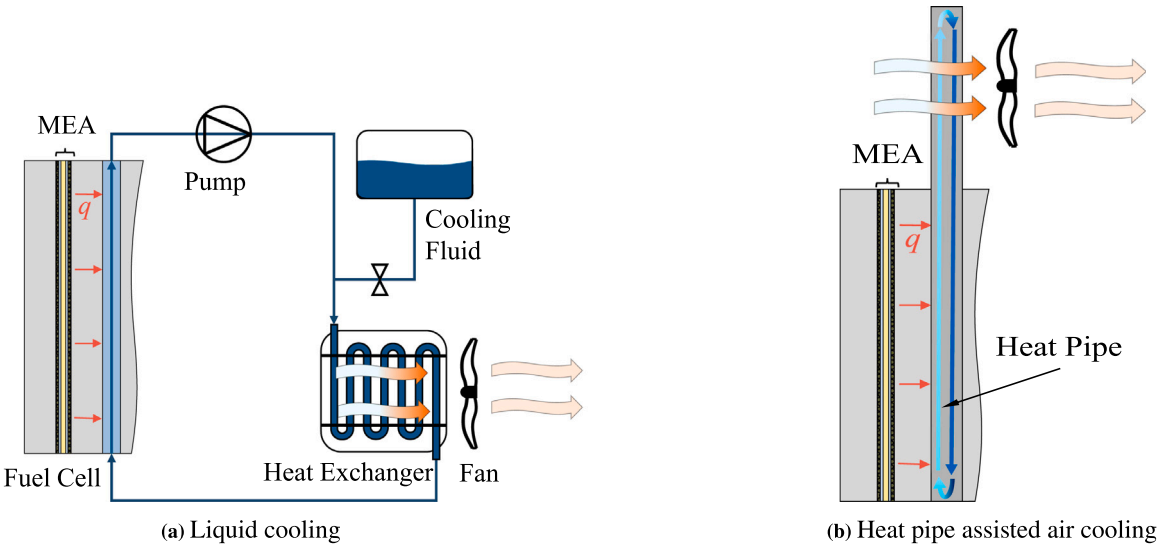

Fig. 1. Comparison of two TMS schematics.

In this case study, a heat transfer concept for fuel cells is introduced, employing a particular kind of heat pipe called a Pulsating Heat Pipe (PHP). The PHP is used to transfer heat from a HT-PEM fuel cell stack to an external airflow, as shown in Fig. 1b. The goal is to ensure that the cell remains colder than 200 °C and to homogenize the fuel cell stack temperature, while simultaneously eliminating the need for a coolant pump and reducing parasitic compressor power.

The PHP, also called Oscillating Heat Pipe (OHP) is a special kind of heat pipe and was first introduced by Akachi [20] in 1990. It consists of a closed capillary tube that is bent into winding turns, often referred to as meanders, and is filled with a working fluid and its vapor. During operation the heat transfer inside a PHP is driven by the motion of liquid plugs and vapor slugs inside the capillary meanders. This self sustained, pulsating motion occurs due to evaporation of liquid and the expansion of vapor slugs on the hot side of the systems as well as condensation and vapor contraction on the cold side. A section of a simplified PHP with a single strand visualizing the working principle is depicted in Fig. 2.

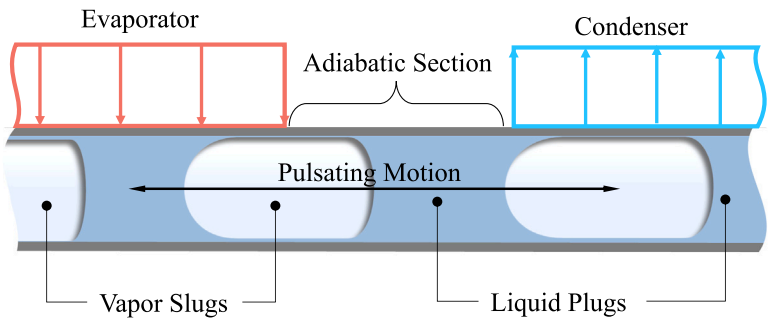

Fig. 2. Working principle of a single strand PHP.

The thermodynamic and hydrodynamic mechanisms underlying heat transfer in a PHP are very complex. These mechanisms include thin-film deposition and evaporation, variations in contact angles and capillary forces between the menisci of liquid plugs and channel walls, the pipe orientation relative to gravity, nucleate boiling, and viscous friction at the channel walls [21]. Hence, despite the apparent simplicity of the PHP system, the detailed processes governing its heat transfer behavior are not entirely understood yet and are the focus of numerous research efforts [22–26].

A Distinguishing characteristic of a PHP is an inner hydraulic diameter D, which is smaller than a given critical Diameter D_{crit}. This critical diameter is defined by the properties of the selected working as

$$D \leq D_{crit} = 2\sqrt{\frac{\sigma}{(\rho_l - \rho_g)g}}\,. \tag{1}$$

where σ corresponds to the surface tension, ρ_l, ρ_g stand for the density of the working fluid in liquid and gaseous state respectively, while g represents acceleration due to gravity [21,27,28].

A wide range of PHPs have been proposed, developed, and tested, with numerous studies examining the effects of different parameters on thermal performance. According to Han et al. [21] three categories of factors significantly influence the performance of PHPs. A brief overview of the existing literature in the field is given below, organized with respect to these categories.

- Geometric parameters have been shown to play a significant role, including the shape of the cross section – such as circular [29,30], rectangular [31,32], and triangular geometries [33] – as well as the diameter of the channels, the lengths of the evaporator and condenser sections, and the number and shape of meanders [34]. Some configurations have also explored the integration of passive flow control elements like check valves and Tesla valves [35].
- Operational parameters have likewise been extensively studied. These include the temperature levels applied to the system, the magnitude of the heat flux, the type of heat sink employed, and the device orientation with respect to gravity [32,36,37].
- Finally, the choice of working fluid significantly affects performance, with water, ethanol, and acetone being among the most commonly used. The filling ratio of the working fluid has also been identified as a critical parameter [31,38].

For a comprehensive overview of studies conducted in this field, it is referred to Zhang et al. [28] and Ayel et al. [39].

While heat pipes have been widely explored for thermal management in many sectors, several studies have also investigated their application within small fuel cell stacks, demonstrating the feasibility of using these systems to transfer heat to external heat sinks [12,40–42]. Building on these approaches, this work introduces a novel (PHP) design [43] characterized by a hexagonal cross section. To the authors knowledge, this unique combination of geometric configuration and application within a fuel cell stack is unprecedented and offers significant opportunities for further investigation. Implementing a hexagonal cross-section for the PHP is expected to offer several advantages over alternative cross-sectional geometries and other passive fuel cell cooling approaches. One potential benefit of the hexagonal approach is the enabling of a new manufacturing process. Unlike conventional manufacturing methods that rely on milling flat plates or bending metal tubes, the proposed design can be fabricated using a stamping and welding process of metal plates. This would result in very thin PHP walls leading to lighter and smaller systems, while also decreasing manufacturing cost for large production volumes. Furthermore, the hexagonal shape provides increased mechanical stability and rigidity for the fuel cell stack and may also enhance heat transfer within the pipe when compared to circular or rectangular cross sections. Increased heat transfer may occur due to a higher number of boiling nucleation sights, increased capillary pumping in the corners with resulting edge wetting in the evaporator section as well as liquid transport to the evaporator [44,45]. However, the thermodynamic and fluid mechanical characteristics in hexagonal cross sections are only conjecture at this point and will be studied in detail in upcoming experimental investigations.

In addition, previous studies investigating PHPs as a means for cooling fuel cells have mounted the heat pipes adjacent to or in between bipolar plates. This study however investigates the integration of the cooling system into the bipolar plates and in contact with the MEA, decreasing heat transfer distance and reducing the number of components for a fuel cell stack as well as its thickness. These properties could significantly enhance the viability of this thermal management approach and may enable its application for high-power stacks.

The integrated heat pipe concept is described and its working principle specified. A preliminary investigation of its thermal properties and the resulting impact on fuel cell operation is carried out based on a simplified numerical thermal model and literature references. Subsequently, a parameter study is executed to assess the impact of condenser section length and operational changes. The results of the parameter variation are utilized to determine the overall feasibility of the concept and develop a functional demonstrator to define the boundary conditions for future detailed modeling and physical experimentation.

2. Problem description and thermal modeling

A simplified one-dimensional thermal model is developed and parameter variations are conducted to evaluate the concept's feasibility under different conditions. The feasibility of the thermal system is defined by its capability to limit the maximum cell temperature to 200 °C. Further indicators of performance are the homogeneity of the temperature across the membrane, the size of the system and the air flow required for the external heat dissipation.

In a HT-PEM fuel cell most of the heat is generated in the catalyst layers of the MEA [46,47]. As the different layers of the MEA are very thin, it is assumed that the heat is generated uniformly across the MEA. A schematic of a basic fuel cell depicting the multiple layers as well as additional components of the fuel cell system is given in Fig. 3.

2.1. Geometry of PHP-integrated bipolar plate

With the proposed configuration, depicted in its cross section in Fig. 4(b), the heat pipe is in direct contact with the heat source to facilitate heat transfer. The walls of neighboring heat pipe meanders enclose a defined space that serves as a reactant channel. In this manner, the heat pipe serves a dual purpose: managing heat and distributing the reactants and products for the chemical reactions across the MEA.

This way, the heat pipe is built into the structure of the Bipolar Plate (BPP). On the upper side of the membrane, which constitutes the anode side, the hydrogen channels are located, while at the cathode side on the bottom the air channels are placed. The gaseous product water is expelled through the cathode side air channels along with surplus Oxygen and Nitrogen.

To ensure reactant supply to all channels, two tapers are integrated into each meander of the PHP. This generates a parallel flow field along the MEA. It is to be noted that this fuel distribution is unlikely to yield ideal reaction results, in terms of fuel utilization

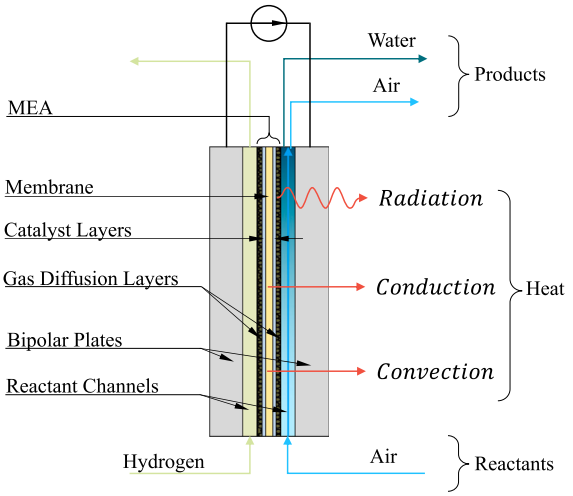

Fig. 3. Schematic of a polymer electrolyte membrane fuel cell, [17].

and efficiency, because of uneven reactant concentrations across the channels. Future design iterations will address this challenge by integrating additional tapers and expanding the flow field pattern. First however, the functionality of the underlying thermal concept is to be validated.

To reduce complexity and minimize calculation time, a singular hexagonal pipe in the center of the PHP-integrated BPP is examined. The system is divided into two sections: the evaporator section within the fuel cell stack and the condenser section, which extends beyond the stack and is immersed in an external air flow. Depictions of singular pipes are shown below. Fig. 5 depicts the simplified geometry of a single strand from the proposed hexagonal pipe, which coincides with the geometry that was applied for the calculations executed in this study.

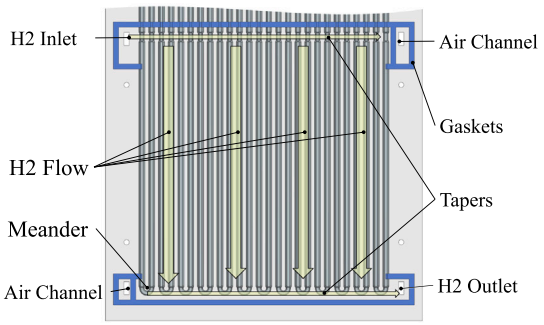

(a) Top view of PHP-BPP with 13 integrated u-shaped meanders

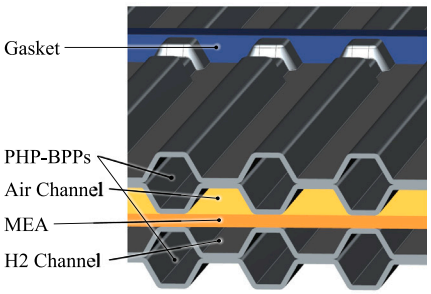

(b) Cross section of MEA-assembly with two PHP-BPPs and gasket

Fig. 4. Top view (a) and cross section (b) of the evaporator section of a PHP-integrated BPP.

As multiple MEAs and BPPs are assembled on top of each other to form a stack, the slice of the evaporator section depicted in Fig. 5 is repeated periodically in y and z direction. In this way the heat transfer in these directions across the boundaries of the calculation domain will be equal to zero if equivalence of the neighboring slices is assumed [48, pp. 112]. As a consequence, the only heat transfer considered in the evaporator section will be along the x-direction. Furthermore, the temperature of a cross section at a given location y_i is assumed to be constant for the MEA, the pipe and the reactant channels.

The goal of these calculations is to assess the temperature distribution along the x-axis for a singular PHP. From the calculated temperature distribution the two key figures of merit, namely the maximum cell temperature and the temperature gradient can be deduced. These values mainly determine the efficacy of the proposed system as an approach to cool HT-PEM fuel cells can be evaluated.

2.2. Assumptions

The assumptions employed to enable calculations and facilitate efficient parameter studies are:

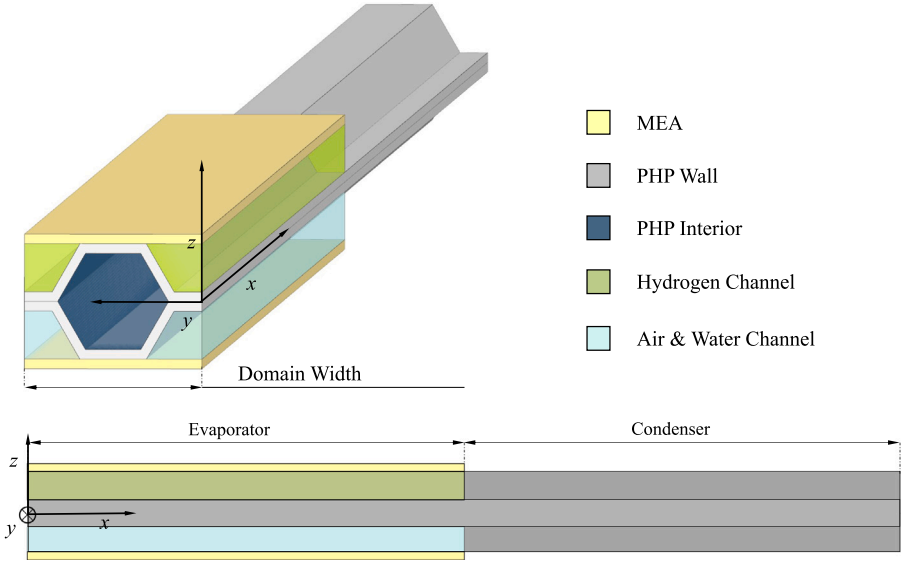

Fig. 5. Simplified geometry of simulation calculation domain including a singular PHP and two MEAs.

- Temperature is constant across the cross section, (1D-approach)
- No heat transfer occurs between neighboring channels or BPPs, (Due to symmetry [48, pp. 112])
- Radiative heat transfer to the environment is neglected,
- The ends of the pipe in x-direction are adiabatic,
- Reactant gases are preheated to operating temperature,
- Heat generation is assumed to be uniformly distributed across the MEA,
  A maximum generation rate of $\dot{w}_{MEA} = 1\,\mathrm{W\,cm^{-2}}$, which is achievable by state-of-the-art MEAs, is applied [49–51],
- The external flow around the condenser section consists of dry air, and a constant velocity in y-direction across all meanders,
- The cooling air channel is assumed to be sufficiently wide to ensure uniform flow. This assumption aligns with the conditions of the planned initial experimental investigations,
- The PHP is considered as a closed system with constant heat capacity, density and equivalent thermal conductivity λ_{eq}.
- The inner diameter of the hexagonal pipe is designed to be 2 mm wide in order to align with the hydraulic diameter of a large number of PHP studies. This facilitates comparability of later experimental results.
- The length of the evaporator section is set to be 10 cm, because many commercial MEAs are available in this size and the first demonstrator will accommodate these membranes.

Whenever possible, assumptions have been deliberately chosen to be conservative, ensuring that factors contributing to heat dissipation are consistently underestimated rather than overestimated. This approach minimizes the risk of producing overly optimistic results, thereby ensuring a more reliable basis for conclusions in the feasibility analysis.

Although the transfer of thermal energy in a heat pipe involves a combination of conduction, convection, fluid transport and phase change processes, the system is frequently regarded as a solid with an equivalent thermal conductivity λ_{eq} defined as

$$\lambda_{eq} = \frac{\dot{Q}\,\Delta x}{A_Q\,\Delta T}\,, \tag{2}$$

where $\dot{Q}$ is the heat transfer rate supplied to the system, A_Q the area over which the heat is spread, and Δx and ΔT are the distance between two points and the difference in temperature.

This perspective establishes λ_{eq} as a metric for assessing the performance of heat pipes as a closed system [33,37]. Another commonly used metric to express thermal performance is the thermal resistance R_{th} of the system

$$R_{th} = \frac{\Delta T}{\dot{Q}}\,, \tag{3}$$

which relates heat transfer rate $\dot{Q}$ to temperature difference ΔT.

While thermal resistance is closely related to equivalent thermal conductivity and is effective for system-level analysis, it does not inherently scale with variations in the underlying geometry. Consequently, equivalent thermal conductivity is selected as the primary metric in this study to enable a parameter analysis involving changes in system length.

The equivalent thermal conductivity and thermal resistance of a given PHP remain challenging to predict due to the extensive range of influencing factors and the complex, time-dependent physical interactions involved. In recent years, advancements in

understanding the governing physical processes have led to improvements of numerical models [52–58]. While the agreement between simulations and experimental data has improved and in some cases shows good alignment, the predictive reliability remains limited when accounting for variations in geometry or operating conditions [36,59].

Therefore, this study relies on thermal performance data for PHP systems available in literature. Reported equivalent thermal conductivities of PHPs vary widely, reflecting the diverse design parameters and experimental conditions of the respective systems. Measured values range from 600 to 10 000 $\mathrm{W\,m^{-1}\,K^{-1}}$ [35,39,60,61].

2.3. Governing equations

The problem is reduced to a one-dimensional conduction model divided into two connected sections. These two sections constitute the evaporator and condenser side of the integrated PHP. The following chapter outlines the application of the heat conduction equation to both sections as well as the heat sources and sinks as they pertain to the evaporator and condenser. For the heat sink on the condenser side an analytical-empirical model is applied, which is subsequently validated in Section 2.3.3 to ensure valid calculation results for the heat sink. After deriving the PDEs for heat conduction in the PHP, the subsequent sections address their numerical treatment. Section 2.4 describes the discretization procedure and the applied boundary conditions. Section 2.5 then introduces the computational solver as well as the model inputs.

2.3.1. Evaporator section

The first section represents the evaporator, where heat is transferred to the heat pipe from the MEA, hydrogen channels and air channels. Under these conditions and according to [48, p. 109], the partial differential equation governing heat conduction with in the evaporator section is expressed as

$$\rho c \frac{\partial \vartheta_I}{\partial t} = \lambda_{eq} \frac{\partial^2 \vartheta_I}{\partial x^2} + \frac{\partial\, w_{Amb}}{\partial t} \frac{W_D}{A_{c,PHP}} + \frac{\partial\, w_{H_2}}{\partial t} + \frac{\partial\, w_{Air}}{\partial t}\,, \tag{4}$$

where ρ denotes the averaged density of the PHP, c is the specific heat capacity and ϑ_I represents the temperature distribution along the x-axis in the evaporator. The terms w_{MEA}, w_{H2} and w_{Air} correspond to the heat in the membrane, the hydrogen channels and the air channels respectively, while λ_{eq} is the equivalent thermal conductivity of the PHP and W_D denotes the width of the calculation domain depicted in Fig. 5.

Heat is applied uniformly across the calculation domain in the evaporator section at a rate of $\dot{w}_{MEA} = 1\,\mathrm{W\,cm^{-2}}$. To determine the resulting MEA-heat flux per volume of the PHP, the heat flux density $\dot{w}_{MEA}$ is multiplied by the ratio of the width of the calculation domain W_D and the cross-sectional area $A_{c,PHP}$ of the heat pipe.

Hydrogen and air are fed into the channels at the MEA to provide the reactants for the redox reactions, but in doing so also heat up due to the proximity to the hot membrane and thereby can contribute to removing the heat fluxes $\dot{w}_{H2}$ and $\dot{w}_{Air}$ from the considered domain.

While this thermal impact can be significant for thermal balance and temperature distribution of a fuel cell and in some cases is sufficient as a stand-alone thermal management approach, [7,62] it is also highly dependent on the operating parameters of the fuel cell. e.g. the fuel utilization, stoichiometry, operating pressure and reactant gas inlet temperature.

If the gases are presumed to be preheated to the target operating temperature of the fuel cell, the thermal impact of these gas flows diminishes. For the calculations in this work the PHP is considered as the central means for heat rejection and therefore the additional cooling due to reactant mass flows is neglected to retain a conservative evaluation of the thermal capability of the proposed system.

2.3.2. Condenser section

The second section represents the condenser, where heat is transferred to an external airflow through forced convection. The end of the condenser section is considered to be adiabatic and no heat conduction to adjacent systems occurs. As a consequence, the one-dimensional heat conduction with a distributed heat source or sink in this section is formulated as

$$\rho c \frac{\partial \vartheta_{II}}{\partial t} = \lambda_{eq} \frac{\partial^2 \vartheta_{II}}{\partial x^2} - \frac{\partial\, w_{Amb}}{\partial t}\,, \tag{5}$$

with ρ, λ_{eq} and c representing the density, equivalent thermal conductivity and specific heat capacity of the PHP, ϑ_{II} being the temperature of the PHP in the condenser section. The heat flux to the environment is given by the change of the thermal energy w_{Amb} with respect to time.

The heat transfer per PHP-volume to the environment is given as

$$\frac{\partial\, w_{Amb}}{\partial t} = \alpha_{conv} \frac{A_{S,PHP}\left(\vartheta_{II} - \vartheta_{Amb}\right)}{V_{PHP}}\,, \tag{6}$$

where α_{Amb} is the heat transfer coefficient, $A_{S,PHP}$ is the surface area of the heat pipe that is in contact with the air flow, V_{PHP} is the volume of the pipe and ϑ_{II} and ϑ_{Amb} are the temperatures of the pipe and the air flow respectively. The external airflow is assumed to have a constant inlet temperature along the x-direction.

Through the years many researchers have developed a wide variety of approaches to calculate the heat transfer coefficients for problems with forced convection. A variety of these methods that are mostly based on empirical calculations are applied for bodies with different geometries as well as a range of flow regimes, represented by the Reynolds and Prandtl Numbers [63].

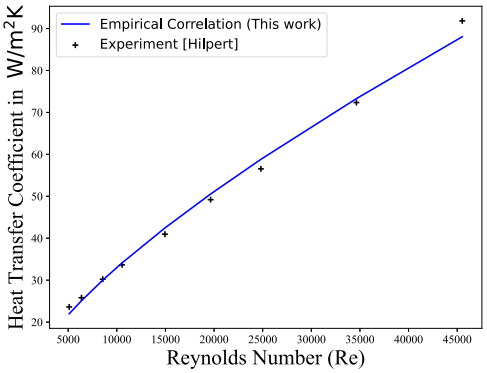

(a) Comparison of heat transfer coefficients from experiment with hexagonal pipe [66] and empirical correlation

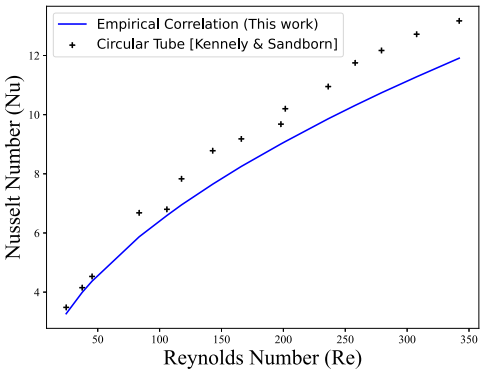

(b) Comparison of Nusselt numbers from experiment with heated circular tube [64] and empirical correlation

Fig. 6. Validation of heat transfer coefficient calculation and Nusselt number for hexagonal (a) and circular (b) cross sections.

In this work, a correlation for prismatic objects with varying cross section shapes in cross flow is selected. The method was developed using the flow-path-length as the designated characteristic length [64,65, pp. 839]. In accordance with this selection a combined Nusselt number Nu_{comb} is calculated from Nu numbers for the laminar Nu_{lam} and turbulent Nu_{turb} flow regimes as

$$Nu_{lam} = 0.664\sqrt{Re}\sqrt[3]{Pr}\,, \tag{7}$$

$$Nu_{turb} = \frac{0.037\,Re^{0.8}\,Pr}{1 + 2.443 Re^{-0.1}\,(Pr^{2/3} - 1)}\,, \tag{8}$$

$$Nu_{comb} = 0.3 + \sqrt{Nu_{lam}^2 + Nu_{turb}^2}\,. \tag{9}$$

With the derived Nusselt number, the heat transfer coefficient α_{conv} can then be calculated, which is applied to determine the heat transfer from the pipe to the airflow. When the investigated object is heated, as in this case, a correction factor K_G is introduced to account for the temperature-dependent changes in the fluid's material properties, such as heat capacity, density and thermal conductivity. For air as the working fluid, this correction factor is determined by

$$K_G = \left(\frac{\vartheta_{\mathrm{Amb}}}{\vartheta_{\mathrm{II}}}\right)^{0.12}\,. \tag{10}$$

This factor is then multiplied with the calculated heat transfer coefficient α_{conv} to gain a more accurate representation of the heat transfer occurring at the object's surface. Hence, for higher PHP-wall temperatures, the heat transfer coefficient decreases.

Additional adjustments are required if the surrounding air channel is marginally larger than the investigated object. However, in this study and the experimental work used for validation [64,66], the air channels are significantly larger than the tested objects, and such adjustments are therefore not applied. The validation of the heat sink model is carried out in the following Section 2.3.3. If future work involves integrating the heat pipe into a stack, thereby altering the dimensional relationship, this consideration will need to be addressed.

2.3.3. Validation of the condenser heat sink model

To assess whether the analytical-empirical calculation of convective heat transfer presented above produces results that accurately reflect reality, the method was applied to cases with existing physical measurements. Two studies were selected for this purpose, and the simulation was repeated under the conditions specified in each experiment. For lower Reynolds numbers, a study investigating a circular heated pipe in cross flow [64] was chosen, as no study with a shape more closely resembling the geometry of interest could be found. For higher Reynolds numbers, a study involving a hexagonal pipe was selected [66], as its shape more closely resembles the geometry of the simulated single heat pipe abstraction. Fig. 6 illustrates the comparison between the measured and simulated results.

For low Reynolds numbers and a circular cross section, the calculation shows reasonable agreement with the measured data, but significant deviations occur, resulting in an average error of 9.5%, as seen in sub Fig. 6(b). For this case, the comparison was conducted with the Nusselt number instead of the more applicable heat transfer coefficient, because the experimental source did not supply the necessary context to accurately derive the heat transfer coefficient.

In contrast, for the hexagonal pipe the simulated heat transfer aligns very well with the measured data, as shown in sub Fig. 6(a). The progression of the simulated transfer coefficients closely follows the trend of the data points from [66], with an average difference of 3.1%.

While the close proximity of the experimental data with the empirical heat transfer correlation provides a certain measure of validation for the applied calculation method, it is noted that the boundary conditions of the experiments executed by Hilpert [66] and the application on the 1D model, executed for this research, differ. The experiments were executed using a larger perfectly hexagonal pipe, which was heated uniformly, but the application for this model is a lot smaller, is only heated on one side and merely approximates a hexagonal shape. Therefore, the application of the empirical correlation given above may yield larger errors for the specific application in this research than the ones depicted in Fig. 6.

2.4. Discretization and boundary conditions

To solve the given Partial Differential Equations (PDEs), an implicit finite-difference scheme based on Crank–Nicolson [67] was employed.

Although analytical solutions for the linear PDE in the evaporator section and the nonlinear PDE in the condenser section exist, the finite difference method was chosen to enable the model's extension to account for additional heat sources and more complex conductive behavior within the PHP. The analytical solutions are merely used to verify the resulting temperature distributions. The partial derivatives from the heat conduction equation for the evaporator (subscript I) and the condenser (II) can be approximated using finite differences. The derivative with respect to time is given in Eq. (11), while Eq. (12) represents the second spatial derivative.

$$\frac{\partial \vartheta_{(I/II)}}{\partial t} = \frac{\vartheta^{n+1}_{(I/II);\,i} - \vartheta^{n}_{(I/II);\,i}}{\Delta t} + \mathcal{O} \tag{11}$$

$$\frac{\partial^2 \vartheta_{(I/II)}}{\partial x^2} = \frac{\vartheta^{n+1}_{(I/II);\,i-1} - 2\vartheta^{n+1}_{(I/II);\,i} + \vartheta^{n+1}_{(I/II);\,i+1}}{\Delta x^2} + \mathcal{O} \tag{12}$$

In this context the terms on the left-hand side are the derivatives as they are formulated in Eqs. (4) and (5), while the right-hand side is the discretized approximation that is employed for numerical calculations. ϑ^n_i stands for the temperature at spatial location i and time step n. The notation $i+1$ refers to the adjacent spatial point, while $n+1$ indicates the subsequent time step. Here, Δt represents the time step interval and Δx represents the spatial discretization step size.

By discretizing the heat conduction Eqs. (4), (5) using the approximations in Eqs. (11) and (12) and disregarding higher-order terms as well as the negligible heat fluxes specified in the assumptions, the formulation for the evaporator amounts to

$$\frac{\vartheta^{n+1}_{(I)\,i} - \vartheta^{n}_{(I)\,i}}{\Delta t} = \frac{\lambda_{eq}}{\rho c}\frac{\vartheta^{n+1}_{(I)\,i-1} - 2\vartheta^{n+1}_{(I)\,i} + \vartheta^{n+1}_{(I)\,i+1}}{\Delta x^2} + \frac{\partial w_{MEA}}{\partial t}\frac{1}{\rho\, c}\frac{W_D}{A_{c,PHP}}\,. \tag{13}$$

And the heat conduction equation for the condenser is written as

$$\frac{\vartheta^{n+1}_{(II)\,i} - \vartheta^{n}_{(II)\,i}}{\Delta t} = \frac{\lambda_{eq}}{\rho c}\frac{\vartheta^{n+1}_{(II)\,i-1} - 2\vartheta^{n+1}_{(II)\,i} + \vartheta^{n+1}_{(II)\,i+1}}{\Delta x^2} - K_G\frac{\partial w_{Amb}}{\partial t}\frac{1}{\rho\, c}\frac{W_D}{A_{c,PHP}}\,. \tag{14}$$

Instead of using two separate equations to describe the sections affected by a heat sink and a heat source it is also possible to combine them. This makes it easier to apply numerical algorithms and boundary conditions. In order to join the calculations, the locations at which the heat source and heat sink terms are applied need to be limited to the required locations along the 1D-pipe.

For this purpose, two vectors of i-indices, referring to locations on the PHP, are defined. These determine the ranges of the two sections. For the evaporator this is the membrane length $\vec{i}_{ev} = \{i_0, \ldots, i_{ev_{max}}\}$ and for the condenser the range amounts to $\vec{i}_{con} = \{i_{con_{min}}, \ldots, i_{con_{max}}\}$. The start and end values of each are defined as inputs in the calculation and can be varied to execute parameter studies.

The combined formulation including the range limitations is written as

$$\frac{\vartheta^{n+1}_{i} - \vartheta^{n}_{i}}{\Delta t} = \frac{\lambda_{eq}}{\rho c}\frac{\vartheta^{n+1}_{i-1} - 2\vartheta^{n+1}_{i} + \vartheta^{n+1}_{i+1}}{\Delta x^2} + \underbrace{\frac{\partial w_{MEA}}{\partial t}\frac{1}{\rho\, c}\frac{W_D}{A_{c,PHP}}\vec{i}_{ev}}_{\text{for } i_0 \le i \le i_{ev,max}} - \underbrace{K_G\frac{\partial w_{Amb}}{\partial t}\frac{1}{\rho\, c}\vec{i}_{con}}_{\text{for } i_{con,min} \le i \le i_{con,max}}\,. \tag{15}$$

To facilitate matrix operations, the fused equation is rearranged, isolating the terms containing the temperature values of the subsequent time step $n+1$ as

$$\vartheta^{n+1}_{i}\left(-\frac{1}{\Delta t} - \frac{2\,\lambda_{eq}}{\rho c\,\Delta x^2}\right) + \frac{\lambda_{eq}}{\rho c}\left(\frac{\vartheta^{n+1}_{i-1}}{\Delta x^2} + \frac{\vartheta^{n+1}_{i+1}}{\Delta x^2}\right) = -\frac{1}{\Delta t}\vartheta^{n}_{i} - \frac{\partial w_{MEA}}{\partial t}\frac{1}{\rho\, c}\frac{\vec{i}_{ev}}{\rho\, c}\frac{W_D}{A_{c,PHP}} + K_G\frac{\partial w_{Amb}}{\partial t}\frac{1}{\rho\, c}\frac{\vec{i}_{con}}{\rho\, c}\,. \tag{16}$$

An implicit time-marching scheme is used to solve the heat conduction problem, where the temperature distribution of the PHP changes over time until a steady state, defined by a convergence criterion is reached.

At each time step, which constitutes one second, a system of linear equations is solved to generate the temperature distribution at the next time step $n+1$. To enable the solving of this system, Eq. (16) is rewritten in matrix form:

$$\mathbf{A}\cdot\vec{\vartheta}^{n+1} = \vec{b}\,. \tag{17}$$

Here, **A** is a coefficient matrix based on the spatial and temporal discretization expressed in Eq. (13), as well as the given boundary conditions, and $\vec{\vartheta}^{n+1}$ is the temperature distribution at the next time step. In the vector $\vec{b}$ on the right-hand side, the temperature values from the previous time step ϑ^n are included, along with the location-dependent heat sources and heat sinks.

For an internal point i in the discretized domain, the coefficient matrix **A** is populated as

$$\mathbf{A}[i,i-1] = \frac{\lambda_{eq}}{\rho c\ \Delta x^2}; \quad \mathbf{A}[i,i] = -\left(\frac{1}{\Delta t} + \frac{2\ \lambda_{eq}}{\rho c\ \Delta x^2}\right); \quad \mathbf{A}[i,i+1] = \frac{\lambda_{eq}}{\rho c\ \Delta x^2}\ . \tag{18}$$

As discussed in the assumptions in Section 2.2, Neumann boundary conditions are applied at the ends of the pipe to simulate the adiabatic nature at the border of the calculation domain:

$$\left.\frac{\partial \vartheta}{\partial x}\right|_{x=0} = 0; \qquad \left.\frac{\partial \vartheta}{\partial x}\right|_{x=l} = 0\ . \tag{19}$$

To enforce these conditions, entries in the coefficient matrix **A** corresponding to the temperature values at the ends of the PHP are modified, along with the first entry in the solution vector $\vec{b}$, as detailed in Eqs. (20) and (21). This ensures zero temperature difference at the pipe ends, preventing heat flux across the computational domain boundaries:

$$\mathbf{A}[0,0] = -1; \quad \mathbf{A}[0,1] = 1; \quad \vec{b}[0] = 0\ ; \tag{20}$$

$$\mathbf{A}[nx-1, nx-2] = -1; \quad \mathbf{A}[nx-1, nx-1] = 1; \quad \vec{b}[nx-1] = 0\ . \tag{21}$$

2.5. Model inputs and numerical solution of the discretized PDEs

To execute the script a number of environmental boundary conditions as well as the initial temperature distribution within the PHP are required in addition to the model assumptions given in Section 2.2: The external atmospheric conditions as well as the coolant air speed, the assumed equivalent thermal conductivity and the length of the condenser section. For all simulations the initial temperature was uniformly set to 15 °C.

To solve the discretized numerical time marching scheme, given by Eq. (16), a python script was developed employing the *numpy* package. The solver applies a LU-decomposition to calculate $\vec{\vartheta}^{n+1}$ as described in Eq. (17) [68]. The code also handled the evaluation of the empirical heat sink model for each iteration in the time marching scheme as shown by Eqs. (6)–(10).

2.6. Parametric design study

The objective of this study is to evaluate the thermal performance of the proposed PHP to support the design process. To achieve this goal, various influencing factors need to be considered. Therefore, a large number of simulations are conducted, systematically varying key parameters to assess their impact on the system's thermal performance.

They key indicators of thermal performance for the TMS of a fuel cell are the maximum temperature at the MEA as well as the temperature gradients across the cell. Hence, these values are extracted for each evaluated set of parameters to concisely quantify the thermal behavior.

Critical parameters driving the design process include the dimensions of the fuel cell, particularly the active area and the length of the PHP-BPP. Because commercially available fuel cell membranes will be used for the initial integration tests, the design is based on a standard 100 × 100 mm MEA. Consequently, the evaporator section of the PHP-BPP, which incorporates the reactant channels, will have approximately the same dimensions. Therefore, the condenser length serves as the primary geometric parameter that can be adjusted during the design process.

The performance of the cooling architecture is governed not only by its geometry but also by the operating conditions. Parameters such as the flow velocity and inlet temperature of the coolant air significantly affect the resulting thermal distribution. Therefore, the parameter study will focus on investigating the effects of coolant inlet temperature and flow velocity.

Finally, due to the novelty of the proposed system, its thermal performance – expressed in equivalent thermal conductivity or thermal resistance – remains uncertain. Existing PHP conductivity measurements serve as a baseline for this preliminary study. To determine the required performance for the hexagonal PHP-BPP to be a viable fuel cell cooling solution, the equivalent thermal conductivity of the pipe is investigated as another varying parameter.

3. Results and discussion

The numerical calculation was executed with a location discretization of $\Delta x = 0.1$ mm and a numerical residual $res < 10^{-7}$ for each iteration. Two time step iterations along with the resulting steady state temperature distributions are depicted in Fig. 7. The coolant air inlet temperature was set to 323.15 K to reflect the operational conditions of the system, which is designed for use in aircraft applications. This temperature accounts for the conditions encountered on runways during hot days.

It is evident from sub Fig. 7(a) that for an equivalent thermal conductivity of $\lambda_{eq} = 401\ \mathrm{W\,m^{-1}\,K^{-1}}$ the maximum temperature in the evaporator exceeds the maximum permissible temperature of 473.15 K for a HT-PEM cell. Furthermore, the low conductivity results in a very large temperature gradient ($\Delta T = 83.5$ K) along the 10 cm long evaporator section.

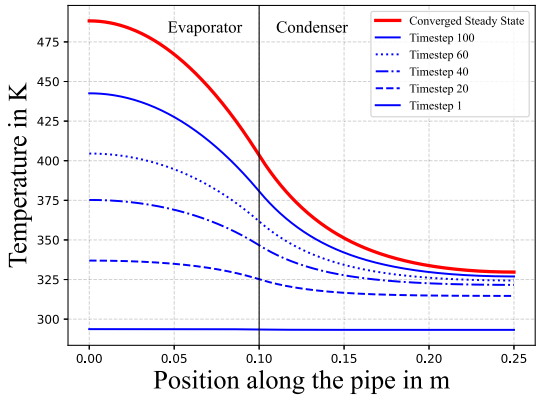

(a) $\lambda_{eq} = 401\,\mathrm{W\,m^{-1}\,K^{-1}}$; Thermal conductivity of copper

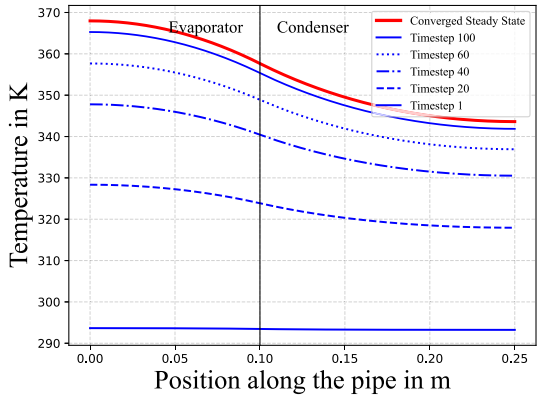

(b) $\lambda_{eq} = 3300\,\mathrm{W\,m^{-1}\,K^{-1}}$, Value of example PHP from literature [61]

Fig. 7. Temperature distribution along the PHP, calculated for two equivalent conductivities (a, b); with condenser length = 0.15 m, coolant air speed = $3\,\mathrm{m\,s^{-1}}$ and air temperature = 323.15 K.

Although a temperature gradient does not entirely prevent fuel cell operation, it drastically lowers the performance and leads to quick degradation of the cell. A key factor contributing to degradation under high temperature gradients is the differential thermal expansion within the MEA, which induces thermal stresses. This effect increased by the mismatch in thermal expansion coefficients between the individual layers, possibly leading to delamination. In Addition, large temperature gradients always lead to parts of the fuel cell working in less than ideal temperature regimes, which also speeds up the degradation, especially in the catalyst layers of the MEA [1,69]. Extending the condenser length and increasing airflow velocity may lower the maximum temperature to an acceptable level. However, the large thermal gradients render materials with thermal conductivities comparable to copper unsuitable for the proposed heat spreading and rejection system.

In contrast, when the thermal conductivity of the pipe is increased to a level not achievable by most solid materials the maximum temperature as well as the temperature gradient decrease notably as seen in Fig. 7(b). For an equivalent thermal conductivity of $\lambda_{eq} = 3300\,\mathrm{W\,m^{-1}\,K^{-1}}$, which was measured in a PHP for power electronics application [61], the gradient decreases to 10.1 K. The temperature distribution demonstrates that highly conductive elements such as heat pipes can effectively reduce operating temperature and achieve a degree of temperature homogeneity feasible for long term operation.

3.1. Parameter variation

For the parametric design study, simulations are performed across a wide range of input parameters. The contour plots in Figs. 8 and 9 illustrate the maximum temperature in the evaporator section computed for each parameter set.

Initially, the influence of condenser length is examined in conjunction with equivalent thermal conductivity (Fig. 8(a)) and external airflow velocity (Fig. 8(b)), assuming an environmental temperature of 323.15 K.

From these figures it is evident that a large number of combinations of condenser lengths, conductivity and external air speed exist which keep the maximum temperature below the required threshold of 473.15 K. In the first case, only the combinations with either very low conductivity or small condenser lengths lead to particularly elevated temperatures. Both parameters have similar impact on the maximum temperature and the trade-off between the two parameters are therefore notable, but moderate.

In the second case the interaction is more pronounced and a very steep rise in maximum temperature is calculated for the combination of low air speed and small condenser length. Overall however, the contour also exhibits a large field of parameter combinations resulting in acceptable peak temperatures.

Fig. 9(a) summarizes the effects of varying equivalent thermal conductivity and airflow velocity. Similar to the interaction between airflow velocity and condenser length, the contour plot reveals a wide range of operating conditions that maintain the maximum temperature below the critical threshold of 473.15 K. Overheating of the pipe and, consequently, the MEA occurs only in cases of very low conductivity or when intermediate conductivity is combined with low airflow velocity.

The second thermal result that was investigated with a focus on the impact of the varying parameters is the maximum temperature difference that occurs in the evaporator section, as this will be the part in direct contact with the fuel cell.

In Fig. 9(b) it is striking that the conductivity has a very clear impact on the resulting temperature gradient. A temperature gradient smaller than 10 K is achieved for conductivities of $3400\,\mathrm{W\,m^{-1}\,K^{-1}}$ or higher.

The air flow speed on the other hand, does not impact the achieved temperature difference. This is demonstrated by the identical gradient distributions for varying speeds. For the parameter *condenser length*, the same independence of temperature gradient is evident. Therefore, it can be concluded that while all parameters influence the maximum temperature to different degrees, solely the equivalent thermal conductivity impacts the thermal gradient in pipe-wise direction.

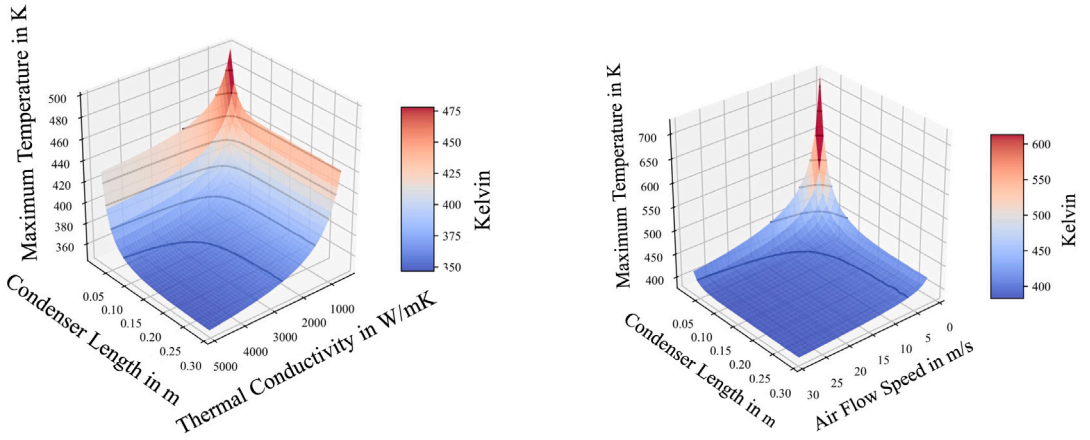

(a) Maximum evaporator temperature with varying λ_{eq} and condenser length; external air speed = 10 m s^{-1} at 323.15 K

(b) Maximum evaporator temperature with varying condenser length and external air speed at 323.15 K; λ_{eq} =1000 W m^{-1} K^{-1}

Fig. 8. Peak temperatures in evaporator section with varying geometrical and operational parameters.

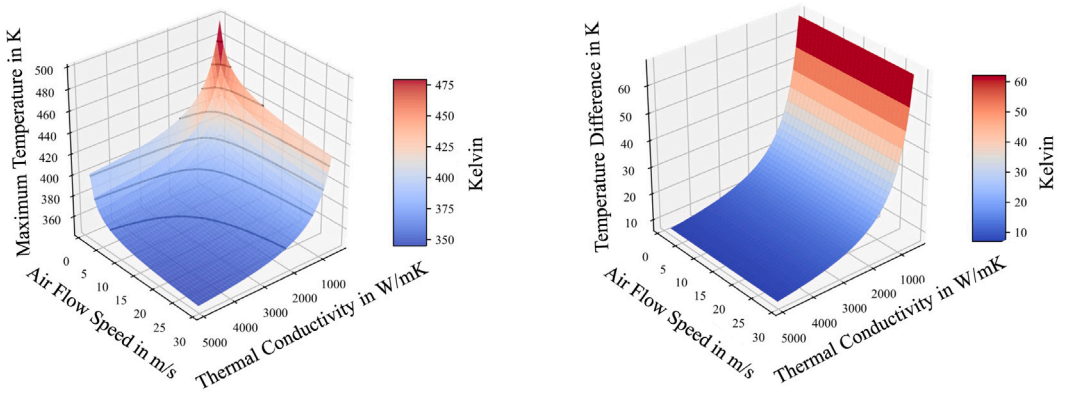

(a) Maximum evaporator temperature with varying λ_{eq} and external air speed at 323.15 K; condenser length = 0.1 m

(b) Temperature difference with varying λ_{eq} and air speed at 323.15 K; condenser length = 0.1 m

Fig. 9. Peak temperature and temperature difference in evaporator section with varying geometrical and operational parameters.

The parametric design study results in a plethora of design points, many of which meet the requirements for maintaining maximum temperature below the given threshold. To provide a concise quantitative overview, selected parameter pairs are summarized in Table 1. For each case, the minimum value of the corresponding third parameter required to satisfy the maximum temperature constraint is also reported.

3.2. Air flow temperature

The final critical parameter for thermal operation is the inlet temperature of the coolant airflow. In the preceding parameter studies, the inlet temperature was set to 323.15 K to simulate conditions on a hot runway. To assess system feasibility in different environments and account for thermal impacts from nearby heat sources, as in closely arranged meanders within a PHP-BPP, temperature distributions are calculated for varying inlet temperatures.

The inlet temperature is adjusted, starting at 323.15 K and rising in steps of 3.36 K over 24 increments to 403.79 K. This increase represents the heating of the airflow in a channel ($height_{channel}$ = 1 mm, $\vec{v}_{air}$ = 10 m s^{-1}) as it absorbs waste heat from the fuel cell. The number of increments corresponds to the number of individual pipes in line forming the PHP. Hence, this variation models a system where coolant air is progressively heated by successive condenser sections, as it flows through the cooling channel.

Table 1
Summary of selected parameter pairs and the corresponding minimum value of the third parameter required to keep the maximum temperature T_{max} below 473.15 K.

Parameter pair		Minimum requirement of third parameter
Airflow speed [m/s]	Condenser length [m]	Thermal conductivity [W/m K]
3	0.02	Not possible; $T_{max} > 473.15$
3	0.10	Not possible; $T_{max} > 473.15$
3	0.20	450
10	0.02	760
Airflow speed [m/s]	Thermal conductivity [W/m K]	Condenser length [m]
3	500	0.8
3	3300	0.29
Thermal conductivity [W/m K]	Condenser length [m]	Airflow speed [m/s]
500	0.10	2.8
3300	0.02	5.7

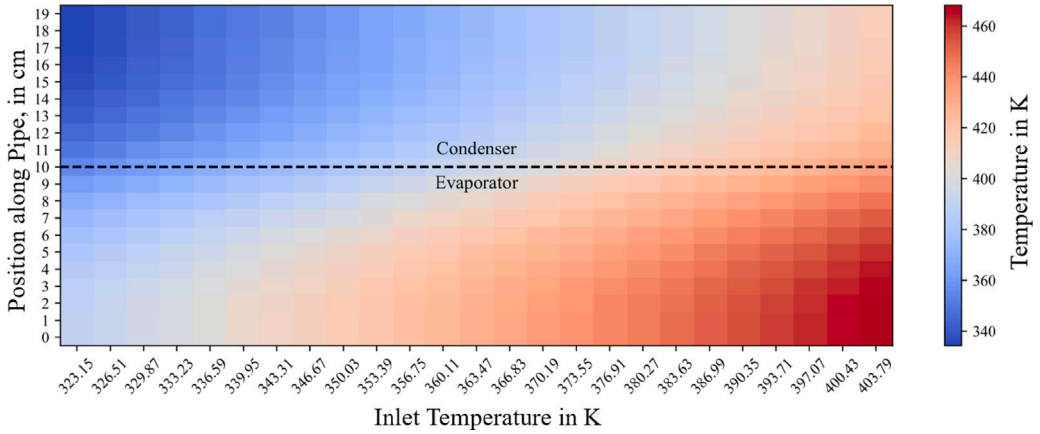

Fig. 10. Temperature distributions for varying inlet temperatures of external coolant flow; air speed = 10 m s^{-1}; λ_{eq} = 1000 W m^{-1} K^{-1}; condenser length = 0.1 m.

The resulting temperature distributions are depicted in Fig. 10. The temperature difference between the hottest and coldest point of every single pipe remains constant across the changing inlet temperatures further underlining the fact that only the conductivity determines the temperature gradient across a single pipe in the evaporator.

Fig. 10 also shows that for inlet temperatures up to 403.79 K, corresponding to the last pipe, the evaporator temperature remains within the permissible limit. At this inlet temperature, the maximum evaporator temperature reaches 468.26 K.

Although the requirement of maximum temperature is met, a large temperature difference of 100.26 K between the hottest spot in the evaporator on the last pipe and the coldest spot on the first pipe can be seen. Such a gradient would prohibit long term operation of the fuel cell. For the planned initial tests this is of little concern, because the tests will be executed in a wide air channel, but when designing a PHP-based TMS for a densely packed fuel stack with narrow coolant channels, strategies to alleviate this gradient will need to be considered. Modifying key parameters such as channel width, airflow velocity, or condenser length presents a potential approach to address this challenge.

3.3. Capabilities and limitations of the applied calculation method

The developed model is able to very quickly calculate the static thermal behavior of a single conducting rod under the boundary conditions of a uniform heat source on the one end and a temperature and environmentally dependent convective heat sink on the other section. The speed and simplicity of the procedure facilitates the quick variation of model inputs to generate a large field of thermal responses. This in turn enables the selection of suitable parameter combinations and the optimization on the model inputs. However, such a simplified approach also has a number of significant drawbacks. The most essential limitation stems from the reliance on conductivity measures from literature. Because of this, the model is unable to predict the true thermal performance within the PHP, but rather just predicts the behavior of the larger system and the heat sink under the assumption of a predetermined equivalent conductivity. As a result, changes to the central geometry of the PHP may not be simulated accurately, where they differ from existing PHPs. Furthermore, a number of inaccuracies are to be expected due to the numerical procedure and the 1D-simplification, which does not take into account varying temperature from the contact surface to the center of the pipe.

Further errors may occur due to the course discretization, which is necessary to execute the wide range of parameter variations. Added to this, there is also the uncertainty of the convective heat sink. While the calculations were validated against a hexagonal rod in a free stream as well as a circular rod, some deviations from the experimental values occurred and the selected pipe shape is not a perfect hexagon, which may induce further differences.

4. Conclusion and outlook

A novel approach for cooling HT-PEM fuel cell stacks is presented utilizing PHPs to transfer heat from the membrane to a coolant air flow. To reduce system mass, volume and parasitic power consumption, a TMS was developed integrating PHPs with hexagonal cross sections into the bipolar plates of a fuel cell stack.

A numerical 1D-model, simulating a single strand of the PHP was developed to evaluate the systems potential thermal performance based on empirical correlations for convective heat transfer and equivalent thermal conductivities of existing PHPs from literature. The model was validated against experimental data of hexagonal and circular heated pipes in a cross flow.

Using the 1D-model, a parametric design study was conducted to analyze the impacts of geometrical and operational factors on the temperature distribution across the length of the pipe. The study was based on a $10\,\mathrm{cm}$ long membrane acting as a uniform heat source in direct contact with the evaporator section of the PHP-BPP. The investigated parameters included: condenser section length, coolant air speed, equivalent thermal conductivity of the PHP and ambient air temperature.

The results confirm that operating conditions can be maintained below the $473.15\,\mathrm{K}$ threshold across a wide range of parameter combinations, underscoring the theoretical feasibility of the proposed thermal system. All investigated parameters significantly affect the maximum temperature, whereas only the equivalent thermal conductivity influences the temperature gradient across the evaporator section. To achieve a temperature gradient of less than $10\,\mathrm{K}$, which serves as a benchmark for long term operation of a HT-PEM fuel cell, an equivalent thermal conductivity larger than $3400\,\mathrm{W\,m^{-1}\,K^{-1}}$ is required. Additionally, for small coolant channels and multiple pipes arranged in a PHP, air heating along the channel results in high temperature gradients in the direction of the flow. Further research is needed to investigate this phenomenon in detail and develop strategies for gradient mitigation. It can be concluded from the simulations and parametric studies that the proposed PHP-assisted air cooling system may present a viable alternative to conventional liquid cooling of HT-PEM fuel cells.

Based on this design study, a demonstrator will be developed to investigate the achievable thermal performance of the system, validate the numerical model and experimentally demonstrate the feasibility of the technology. The system's performance under various environmental conditions will be analyzed, including measures of equivalent thermal conductivity, thermal resistance and localized temperature gradients. The impact of the hexagonal cross section shape on the internal fluid behavior will be investigated and the feasibility of the system for integration into a fuel cell stack will be evaluated. In order to implement a scaled up integrated stack incorporating PHPs, flow fields for the reactant gases will need to be implemented into the structure of the proposed PHP-Bipolar Plate. The electrical conductivity in cross wise direction will need to measured and minimized and gaskets will need to be designed and installed to the MEA-facing sides of the PHP

Furthermore, a high fidelity simulation of the ambient heat transfer will be executed to enhance accuracy and predictive capability of the model introduced in this paper.

Overall, this study demonstrates the potential of PHP-integrated BPPs as a viable option for HT-PEM fuel cell cooling, warranting further experimental research and comparative assessments to conventional cooling architectures.

CRediT authorship contribution statement

Friedrich Franke: Writing – original draft, Visualization, Validation, Software, Methodology, Investigation, Formal analysis, Conceptualization. **Markus Kober:** Writing – review & editing, Visualization, Validation, Supervision, Project administration, Conceptualization. **Stefan Kazula:** Writing – review & editing, Visualization, Supervision, Project administration, Methodology, Conceptualization.

Declaration of competing interest

The authors declare the following financial interests/personal relationships which may be considered as potential competing interests: Friedrich Franke has patent Vorrichtung für eine Brennstoffzelle, Brennstoffzelle und Verfahren zur Herstellung einer Vorrichtung pending to Deutsche Patent- und Markenamt. Stefan Kazula has patent Vorrichtung für eine Brennstoffzelle, Brennstoffzelle und Verfahren zur Herstellung einer Vorrichtung pending to Deutsche Patent- und Markenamt. If there are other authors, they declare that they have no known competing financial interests or personal relationships that could have appeared to influence the work reported in this paper.

Data availability

Data will be made available on request.

References

[1] Q. Li, High Temperature Polymer Electrolyte Membrane Fuel Cells: Approaches, Status, and Perspectives, Springer International Publishing, Cham, 2015.

[2] Y. Huang, X. Xiao, H. Kang, J. Lv, R. Zeng, J. Shen, Thermal management of polymer electrolyte membrane fuel cells: A critical review of heat transfer mechanisms, cooling approaches, and advanced cooling techniques analysis, Energy Convers. Manage. 254 (2022) 115221, http://dx.doi.org/10.1016/j.enconman.2022.115221.

[3] A. Baroutaji, A. Arjunan, M. Ramadan, J. Robinson, A. Alaswad, M.A. Abdelkareem, A.-G. Olabi, Advancements and prospects of thermal management and waste heat recovery of PEMFC, Int. J. Thermofluids 9 (2021) 100064, http://dx.doi.org/10.1016/j.ijft.2021.100064.

[4] Q. Li, Z. Liu, Y. Sun, S. Yang, C. Deng, A review on temperature control of proton exchange membrane fuel cells, Processes 9 (2) (2021) 235, http://dx.doi.org/10.3390/pr9020235.

[5] J. Bai, H. Fan, S. Cui, L. Wang, S. He, M. Chen, H. Zheng, Experimental study of phase change heat dissipation system based on hydrogen fuel cell, Case Stud. Therm. Eng. 59 (2024) 104495, http://dx.doi.org/10.1016/j.csite.2024.104495.

[6] T. song, Kyoung-Hwan. Choi, Ji-Rae. Kim, Jung.S. Yi, Song, Tae, WonSong, K.-H. Choi, J.-R. Kim, J.S. Yi, Pumpless thermal management of water-cooled high-temperature proton exchange membrane fuel cells, J. Power Sources 196 (10) (2011) 4671–4679, http://dx.doi.org/10.1016/j.jpowsour.2010.12.108.

[7] A. de las Heras, F.J. Vivas, F. Segura, M.J. Redondo, J.M. Andújar, Air-cooled fuel cells: Keys to design and build the oxidant/cooling system, Renew. Energy 125 (2018) 1–20, http://dx.doi.org/10.1016/j.renene.2018.02.077.

[8] E.H. Reddy, S. Jayanti, D.S. Monder, Thermal management of high temperature polymer electrolyte membrane fuel cell stacks in the power range of 1–10 kWe, Int. J. Hydrog. Energy 39 (35) (2014) 20127–20138, http://dx.doi.org/10.1016/j.ijhydene.2014.09.132.

[9] E. Harikishan Reddy, S. Jayanti, Thermal management strategies for a 1 kWe stack of a high temperature proton exchange membrane fuel cell, Appl. Therm. Eng. 48 (2012) 465–475, http://dx.doi.org/10.1016/j.applthermaleng.2012.04.041.

[10] T.L. Kösters, X. Liu, D. Kožulović, S. Wang, J. Friedrichs, X. Gao, Comparison of phase-change-heat-pump cooling and liquid cooling for PEM fuel cells for MW-level aviation propulsion, Int. J. Hydrog. Energy 47 (68) (2022) 29399–29412, http://dx.doi.org/10.1016/j.ijhydene.2022.06.235.

[11] J. Wang, Y. Zhu, S. Wang, L. Yue, Z. Qian, Numerical investigatio of high-temperature PEMFC thermal management using pyrolytic graphite, Int. J. Heat Mass Transfer 224 (2024) 125322, http://dx.doi.org/10.1016/j.ijheatmasstransfer.2024.125322.

[12] J. Supra, Kühlkonzepte Für Hochtemperatur- Polymerelektrolyt-Brennstoffzellen-Stacks: Zugl.: Aachen, Techn. Hochsch., Diss., 2014, Schriften Des Forschungszentrums Jülich, Reihe Energie & Umwelt, vol. Bd. 209, Forschungszentrum Zentralbibliothek, Jülich, 2014.

[13] K. Sasiwimonrit, W.-C. Chang, Thermal management of high temperature polymer electrolyte membrane fuel cells by using flattened heat pipes, Therm. Sci. 25 (4 Part A) (2021) 2411–2423, http://dx.doi.org/10.2298/TSCI190324135S.

[14] J. Zhao, Z. Huang, B. Jian, X. Bai, Q. Jian, Thermal performance enhancement of air-cooled proton exchange membrane fuel cells by vapor chambers, Energy Convers. Manage. 213 (2020) 112830, http://dx.doi.org/10.1016/j.enconman.2020.112830.

[15] Y. Han, W. Zhuge, J. Peng, Y. Qian, P. Ming, Y. Zhang, A novel heat pipe bipolar plate for proton exchange membrane fuel cells, Energy Convers. Manage. 284 (2023) 116945, http://dx.doi.org/10.1016/j.enconman.2023.116945.

[16] S.A. Atyabi, E. Afshari, C. Udemu, Comparison of active and passive cooling of proton exchange membrane fuel cell using a multiphase model, Energy Convers. Manage. 268 (2022) 115970, http://dx.doi.org/10.1016/j.enconman.2022.115970.

[17] F. Franke, A. Link, S. Kazula, Evaluation of heat transfer technologies for high temperature polymer electrolyte membrane fuel cells as primary power source in a regional aircraft, CEAS Aeronautical Journal (2025) http://dx.doi.org/10.1007/s13272-025-00908-0.

[18] Momentive Technologies Inc, High thermal conductivity heat sinks, 2024, (Accessed 22 July 2025). URL https://www.momentivetech.com/products/ceramics/thermal-management-products/high-thermal-conductivity-heat-sinks/.

[19] HPMS Graphite, Thermally conductive graphite, 2024, (Accessed 22 July 2025). URL https://hpmsgraphite.com/thermallyconductivegraphite.

[20] H. Akachi, Structure of a heat pipe: United States patent - no. 4921041, 1990, 4921041.

[21] X. Han, X. Wang, H. Zheng, X. Xu, G. Chen, Review of the development of pulsating heat pipe for heat dissipation, Renew. Sustain. Energy Rev. 59 (2016) 692–709, http://dx.doi.org/10.1016/j.rser.2015.12.350.

[22] Y. Huang, R. Bai, X. Chen, H. Li, X. Han, X. Liu, Investigation of thermo-hydrodynamic characteristics in micro-oscillating heat pipe by alternatively-arranged ratchet microchannels, Int. J. Heat Mass Transfer 222 (2024) 125134, http://dx.doi.org/10.1016/j.ijheatmasstransfer.2023.125134.

[23] Y. Li, G. Chang, W. Zhao, Y. Xu, R. Fan, Start-up visualization and performance of flat-plate CLPHP based on PEMFC cooling, Int. J. Heat Mass Transfer 190 (2022) 122553, http://dx.doi.org/10.1016/j.ijheatmasstransfer.2022.122553.

[24] V.S. Nikolayev, Physical principles and state-of-the-art of modeling of the pulsating heat pipe: A review, Appl. Therm. Eng. 195 (2021) 117111, http://dx.doi.org/10.1016/j.applthermaleng.2021.117111.

[25] X. Zhang, V. Nikolayev, Physics and modeling of liquid films in pulsating heat pipes, Phys. Rev. Fluids 8 (8) (2023) http://dx.doi.org/10.1103/PhysRevFluids.8.084002.

[26] M. Schlüter, Local measurement techniques for multiphase flows, Chem. Ing. Tech. 83 (7) (2011) 992–1004, http://dx.doi.org/10.1002/cite.201100039.

[27] Q. Cai, C.-l. Chen, J.F. Asfia, Operating characteristic investigations in pulsating heat pipe, J. Heat Transf. 128 (12) (2006) 1329–1334, http://dx.doi.org/10.1115/1.2349509.

[28] Y. Zhang, A. Faghri, Advances and unsolved issues in pulsating heat pipes, Heat Transf. Eng. 29 (1) (2008) 20–44, http://dx.doi.org/10.1080/01457630701677114.

[29] J.-S. Kim, N.H. Bui, H.-S. Jung, W.-H. Lee, The study on pressure oscillation and heat transfer characteristics of oscillating capillary tube heat pipe, KSME Int. J. 17 (10) (2003) 1533–1542, http://dx.doi.org/10.1007/BF02982332.

[30] T. Katpradit, T. Wongratanaphisan, P. Terdtoon, P. Kamonpet, A. Polchai, A. Akbarzadeh, Correlation to predict heat transfer characteristics of a closed end oscillating heat pipe at critical state, Appl. Therm. Eng. 25 (14–15) (2005) 2138–2151, http://dx.doi.org/10.1016/j.applthermaleng.2005.01.009.

[31] D. Kearney, J. Griffin, An open loop pulsating heat pipe for integrated electronic cooling applications, J. Heat Transf. 136 (8) (2014) http://dx.doi.org/10.1115/1.4027131.

[32] V. Ayel, L. Araneo, A. Scalambra, M. Mameli, C. Romestant, A. Piteau, M. Marengo, S. Filippeschi, Y. Bertin, Experimental study of a closed loop flat plate pulsating heat pipe under a varying gravity force, Int. J. Therm. Sci. 96 (2015) 23–34, http://dx.doi.org/10.1016/j.ijthermalsci.2015.04.010.

[33] Z. Li, L. Jia, Experimental study on natural convection cooling of led using a flat-plate pulsating heat pipe, Heat Transfer Res. 44 (1) (2013) 133–144, http://dx.doi.org/10.1615/HeatTransRes.2012005690.

[34] T. Chen, S. Liu, Y. Shen, B. Gao, A.R. Mazhar, A novel triangular pulsating heat pipe with enhanced heat transfer performance for building energy efficiency, Case Stud. Therm. Eng. 49 (2023) 103286, http://dx.doi.org/10.1016/j.csite.2023.103286.

[35] W.W. Wits, G. Groeneveld, H.J. van Gerner, Experimental investigation of a flat-plate closed-loop pulsating heat pipe, J. Heat Transf. 141 (9) (2019) http://dx.doi.org/10.1115/1.4042367.

[36] M. Abela, M. Mameli, V. Nikolayev, S. Filippeschi, Experimental analysis and transient numerical simulation of a large diameter pulsating heat pipe in microgravity conditions, Int. J. Heat Mass Transfer 187 (2022) 122532, http://dx.doi.org/10.1016/j.ijheatmasstransfer.2022.122532.

[37] F.F. Laun, B. Taft, Experimental investigation of in situ pressure measurement of an oscillating heat pipe, Front. Heat Pipes 5 (2014) http://dx.doi.org/10.5098/fhp.5.8.

[38] C. Kamijima, Y. Yoshimoto, Y. Abe, S. Takagi, I. Kinefuchi, Relating the thermal properties of a micro pulsating heat pipe to the internal flow characteristics via experiments, image recognition of flow patterns and heat transfer simulations, Int. J. Heat Mass Transfer 163 (2020) 120415, http://dx.doi.org/10.1016/j.ijheatmasstransfer.2020.120415.
[39] V. Ayel, M. Slobodeniuk, R. Bertossi, C. Romestant, Y. Bertin, Flat plate pulsating heat pipes: A review on the thermohydraulic principles, thermal performances and open issues, Appl. Therm. Eng. 197 (2021) 117200, http://dx.doi.org/10.1016/j.applthermaleng.2021.117200.
[40] B. Huang, Q. Jian, L. Luo, X. Bai, Research on the in-plane temperature distribution in a PEMFC stack integrated with flat-plate heat pipe under different startup strategies and inclination angles, Appl. Therm. Eng. 179 (2020) 115741, http://dx.doi.org/10.1016/j.applthermaleng.2020.115741.
[41] G. Chang, Y. Li, W. Zhao, Y. Xu, Performance investigation of flat-plate CLPHP with pure and binary working fluids for PEMFC cooling, Int. J. Hydrog. Energy 46 (59) (2021) 30433–30441, http://dx.doi.org/10.1016/j.ijhydene.2021.06.172.
[42] L. Wang, Z. Quan, Y. Zhao, M. Yang, J. Zhang, Experimental investigation on thermal management of proton exchange membrane fuel cell stack using micro heat pipe array, Appl. Therm. Eng. 214 (2022) 118831, http://dx.doi.org/10.1016/j.applthermaleng.2022.118831.
[43] F. Franke, S. Kazula, Antrag auf erteilung eines deutschen patents-2024; Vorrichtung für eine brennstoffzelle, Brennstoffzelle und Verfahren zur herstellung einer vorrichtung: Deutsches patent und markenamt, Anmeldenummer 10 2024 211 417.0, 2024.
[44] H. Yang, S. Khandekar, M. Groll, Operational characteristics of flat plate closed loop pulsating heat pipe, in: 13th International Heat Pipe Conference (13th IHPC), Shanghai, China, September 21-25, 2004, Vol. 2004, 2004.
[45] L. Krambeck, K.G. Domiciano, L.A. Betancur-Arboleda, M.B. Mantelli, Novel flat plate pulsating heat pipe with ultra sharp grooves, Appl. Therm. Eng. 211 (2022) 118509, http://dx.doi.org/10.1016/j.applthermaleng.2022.118509.
[46] J. Ramousse, O. Lottin, S. Didierjean, D. Maillet, Heat sources in proton exchange membrane (PEM) fuel cells, J. Power Sources 192 (2) (2009) 435–441, http://dx.doi.org/10.1016/j.jpowsour.2009.03.038.
[47] S.G. Kandlikar, Z. Lu, Fundamental research needs in combined water and thermal management within a proton exchange membrane fuel cell stack under normal and cold-start conditions, J. Fuel Cell Sci. Technol. 6 (4) (2009) http://dx.doi.org/10.1115/1.3008043.
[48] H.D. Baehr, K. Stephan, Heat and Mass-Transfer-Springer (2006), second ed., Springer, Berlin and Heidelberg, 2006.
[49] Zeroavia, Modular high-temperature PEM fuel cell stack, 2024, URL https://zeroavia.com/in-house-tech/. (Accessed 14 May 2025).
[50] H. Meng, J. Song, P. Guan, H. Wang, W. Zhao, Y. Zou, H. Ding, X. Wu, P. He, F. Liu, Y. Zhang, High ion exchange capacity perfluorosulfonic acid resine proton exchange membrane for high temperature applications in polymer electrolyte fuel cells, J. Power Sources 602 (2024) 234205, http://dx.doi.org/10.1016/j.jpowsour.2024.234205.
[51] Q. Ju, G. Chao, T. Guo, Z. Lv, R. Li, K. Geng, N. Li, Effect of solvent-free membranes-forming processes on HT-PEM properties of highly soluble polybenzimidazole, J. Membr. Sci. 692 (2024) 122264, http://dx.doi.org/10.1016/j.memsci.2023.122264.
[52] M. Mameli, M. Marengo, S. Zinna, Numerical model of a multi-turn closed loop pulsating heat pipe: Effects of the local pressure losses due to meanderings, Int. J. Heat Mass Transfer 55 (4) (2012) 1036–1047, http://dx.doi.org/10.1016/j.ijheatmasstransfer.2011.10.006.
[53] V.S. Nikolayev, M. Marengo, Pulsating Heat Pipes: Basics of Functioning and Modeling, vol. 1, CEA Scientific production, 2021, http://dx.doi.org/10.1142/9789813234406_0002.
[54] G. Rouaze, J.B. Marcinichen, F. Cataldo, P. Aubin, J.R. Thome, Simulation and experimental validation of pulsating heat pipes, Appl. Therm. Eng. 196 (2021) 117271, http://dx.doi.org/10.1016/j.applthermaleng.2021.117271.
[55] H.Y. Noh, S.J. Kim, Numerical simulation of pulsating heat pipes: Parametric investigation and thermal optimization, Energy Convers. Manage. 203 (2020) 112237, http://dx.doi.org/10.1016/j.enconman.2019.112237.
[56] D.-T. Vo, H.-T. Kim, J. Ko, K.-H. Bang, An experiment and three-dimensional numerical simulation of pulsating heat pipes, Int. J. Heat Mass Transfer 150 (2020) 119317, http://dx.doi.org/10.1016/j.ijheatmasstransfer.2020.119317.
[57] P. Aubin, B. D'Entremont, F. Cataldo, J.B. Marcinichen, R.L. Amalfi, J.R. Thome (Eds.), Numerical simulations of pulsating heat pipes, part 1: Modeling, 2019, http://dx.doi.org/10.1109/ITHERM.2019.8757388.
[58] S.M. Pouryoussefi, Y. Zhang, Numerical investigation of chaotic flow in a 2D closed-loop pulsating heat pipe, Appl. Therm. Eng. 98 (2016) 617–627, http://dx.doi.org/10.1016/j.applthermaleng.2015.12.097.
[59] W. Kim, S.J. Kim, Fundamental issues and technical problems about pulsating heat pipes, J. Heat Transf. 143 (10) (2021) http://dx.doi.org/10.1115/1.4051465.
[60] D.S. Jang, D. Kim, S.H. Hong, Y. Kim, Comparative thermal performance evaluation between ultrathin flat plate pulsating heat pipe and graphite sheet for mobile electronic devices at various operating conditions, Appl. Therm. Eng. 149 (2019) 1427–1434, http://dx.doi.org/10.1016/j.applthermaleng.2018.12.146.
[61] D.J. Kearney, O. Suleman, J. Griffin, G. Mavrakis, Thermal performance of a PCB embedded pulsating heat pipe for power electronics applications, Appl. Therm. Eng. 98 (2016) 798–809, http://dx.doi.org/10.1016/j.applthermaleng.2015.11.123.
[62] T. Kurz, J. Keller, Heat management in a portable high temperature PEM fuel cell module with open cathode, Fuel Cells 11 (4) (2011) 518–525, http://dx.doi.org/10.1002/fuce.201000109.
[63] S. Sanitjai, R.J. Goldstein, Forced convection heat transfer from a circular cylinder in crossflow to air and liquids, Int. J. Heat Mass Transfer 47 (22) (2004) 4795–4805, http://dx.doi.org/10.1016/j.ijheatmasstransfer.2004.05.012.
[64] V. Gnielinski, Berechnung mittlerer wärme- und stoffübergangskoeffizienten an laminar und turbulent überströmten einzelkörpern mit hilfe einer einheitlichen gleichung, Forsch. Ingenieurwesen 41 (5) (1975) 145–153, http://dx.doi.org/10.1007/BF02560793.
[65] P. Stephan, S. Kabelac, M. Kind, D. Mewes, K. Schaber, T. Wetzel, VDI-Wärmeatlas, Springer Berlin Heidelberg, Berlin, Heidelberg, 2019, http://dx.doi.org/10.1007/978-3-662-52989-8.
[66] R. Hilpert, Wärmeabgabe von geheizten drähten und rohren im luftstrom, Forsch. Ingenieurwesen 4 (5) (1933) 215–224, http://dx.doi.org/10.1007/BF02719754.
[67] J. Crank, P. Nicolson, A practical method for numerical evaluation of solutions of partial differential equations of the heat-conduction type, Math. Proc. Cambridge Philos. Soc. 43 (1) (1947) 50–67, http://dx.doi.org/10.1017/S0305004100023197.
[68] J.R. Bunch, J.E. Hopcroft, Triangular factorization and inversion by fast matrix multiplication, Math. Comp. 28 (125) (1974) 231, http://dx.doi.org/10.2307/2005828.
[69] J. Wang, S. Wang, Y. Zhu, Y. Wang, Effect of cooling surface temperature difference on the performance of high-temperature PEMFCs, Int. J. Hydrog. Energy 48 (44) (2023) 16813–16828, http://dx.doi.org/10.1016/j.ijhydene.2023.01.125.